



Structural, optical and femtosecond third-order nonlinear optical properties of LiNbO₃ thin films



Anil Tumuluri^a, M.S.S. Bharati^a, S. Venugopal Rao^{a,*}, K.C. James Raju^{a,b,*}

^a Advanced Centre of Research in High Energy Materials (ACRHEM), University of Hyderabad, Hyderabad 500046, Telangana, India

^b School of Physics, University of Hyderabad, Hyderabad 500046, Telangana, India

ARTICLE INFO

Article history:

Received 10 March 2017

Received in revised form 17 June 2017

Accepted 18 June 2017

Available online 19 June 2017

Keywords:

Lithium niobate films

Z-scan

Femtosecond

Optical properties

ABSTRACT

LiNbO₃ thin films were deposited by means of Al:ZnO as intermediate layer using pulsed laser deposition and their structural, linear and nonlinear optical (NLO) properties were investigated. The films were found to be polycrystalline, (110) orientation for Al:ZnO/fused silica and (300) orientation for Al:ZnO/quartz substrates. The films demonstrated a transparency of >80% in the visible and near-infrared region. The NLO studies were performed with the Z-scan technique using ~150 fs, 80 MHz pulses at 800 nm. The studies revealed that the polycrystalline LiNbO₃ films and (300) LiNbO₃ films demonstrated reverse saturable absorption while a transition to saturable absorption was observed in the case of (110) LiNbO₃. The presence of two-photon absorption is attributed to the indirect transition via intermediate defect levels which is related to the structural asymmetry. The large nonlinearity in refractive index could be a result of the strain induced ferroelectric polarization. The magnitude of the third order optical nonlinearity of all films was ~10⁻¹¹ e.s.u. which is orders of magnitude higher than the value obtained for single crystal Z-cut LiNbO₃.

© 2017 Elsevier Ltd. All rights reserved.

1. Introduction

Lithium niobate (LiNbO₃; LN) with its distinct features possesses unique combination of versatile properties such as second-order optical nonlinearity, piezoelectric, ferroelectric, electro-optic, pyroelectric by making this material suitable for wide range of applications like non-linear optical devices, transducers, electro optic modulators and pyroelectric sensors [1–3]. The phenomenal growth in the versatile applications of LiNbO₃ crystals and related compounds reinvigorated further detailed studies. Extensive research has been and is being undertaken on single crystal X-cut, Y-cut and Z-cut LiNbO₃, which demand attention to meet the device requirements. The performance can be enhanced with oriented single crystals of LiNbO₃ [4–6]. Several research groups have focused their research work to integrate and miniaturize devices in to a single platform. For this reason, LiNbO₃ single crystals in diverse orientations are studied and widely used in thin film form by chopping in to thin slices using crystal ion slicing technique [7,8]. Although the advantages are enormous, the

drawbacks of high surface roughness, difficulty in implantation of foreign ions and expensive chopping made it difficult to use them for versatile miniaturized applications [9]. Keeping this in mind, epitaxial LiNbO₃ thin films came in to existence to support the above-mentioned applications. High quality epitaxial LiNbO₃ thin films can be utilized to overwhelm these drawbacks [10,11]. There are numerous reports on the deposition of LiNbO₃ thin films using different techniques like sol-gel, RF magnetron sputtering and pulsed laser deposition are widely available [12–15]. Most of the available literature explains the optimization of deposition conditions for the successful deposition of epitaxial growth of LiNbO₃ thin films with ZnO as buffer layer [16]. Moreover, oriented deposition of LiNbO₃ thin films on amorphous substrates is found to be interesting for many practical purposes. Because of its cost effectiveness, especially, for device applications, LiNbO₃ thin films on amorphous substrates are highly in demand. Higher second order nonlinearity in LiNbO₃ is well studied by several groups and the enhancement factor is reported by using different implantation techniques. However, devoted studies on third order nonlinear optical (NLO) properties of LiNbO₃ thin films are meagre and need to be intensified for finding suitable methodologies rendering them useful in nonlinear photonic devices [17–19]. Ferroelectric materials have been widely investigated for their random-access memory devices, piezoelectric, pyroelectric, integrated photonics

* Corresponding authors.

E-mail addresses: soma_venu@uohyd.ac.in (S. V. Rao), kcjrps@uohyd.ernet.in (K.C. James Raju).

and nonlinear optical applications [20,21]. Among all the ferroelectric materials, LiNbO_3 is a well-studied ferroelectric with high spontaneous polarization and high Curie temperature [22]. Although paramount properties that can be enjoyed in single crystal cannot be reproduced in thin film, the miniaturization of device structure, high quality thin film on desired substrate and ease in doping foreign ions made the researchers to study properties of LiNbO_3 thin films [23]. Studies on deposition of C-axis oriented ferroelectric LiNbO_3 thin films with Al:ZnO as buffer layer are widely reported but their third order nonlinear optical (NLO) properties are not investigated thoroughly [24]. More detailed research studies are essential to investigate the mechanism of third order nonlinearity in LiNbO_3 thin films to utilize them for device structures. Kostritskii et al. measured the nonlinear absorption of congruent LiNbO_3 crystals and observed two-photon absorption associated with the photo dissociation of bipolarons [25]. Henari et al. also recorded the third-order nonlinearity in LiNbO_3 crystal with changing laser beam waist using the Z-scan technique and the calculated nonlinear absorption coefficient (β) which was found to be 5 cm/KW [26]. In the present paper, LiNbO_3 thin films were grown using pulsed laser deposition (PLD) technique and their structural, morphological, emission characteristics along with third-order NLO properties were investigated using femtosecond (fs) pulses and the obtained results are discussed in detail. Large nonlinear refractive index (n_2) values combined with superior second order NLO coefficients will showcase the overall advantages of LiNbO_3 thin films for various photonic applications including all-optical switching and frequency conversion devices.

2. Experimental details

2.1. Materials

In the present study, LiNbO_3 is the material of interest and Al:ZnO was chosen as a buffer layer to control the growth of the top layer. LiNbO_3 and Al:ZnO thin films were produced by PLD (Excel Instruments-Mumbai, India), employing a KrF excimer laser ($\lambda = 248$ nm). The LiNbO_3 target of one inch diameter was prepared from commercially available LiNbO_3 powder (Alfa Aesar, 99.99% purity) by adding 5 wt% of Li_2CO_3 (Sigma Aldrich, 99.99% purity) for Li loss compensation. The $\text{LiNbO}_3 + \text{Li}_2\text{CO}_3$ mixture was pressed using Poly Vinyl Alcohol (PVA) as binder followed by de-binding at 500 °C and sintering at 1100 °C for 2 h. Al:ZnO (Al:0.5 wt%) target of 1 inch diameter was prepared by ball milling Al_2O_3 (purity 99.9%, Alfa Aesar) with ZnO (purity 99.99%, Sigma Aldrich). This mixture

is pressed with PVA as binder followed by de-binding at 500 °C and sintered at 900 °C for 2 h.

2.2. Deposition of LiNbO_3 thin films

Fig. 1 shows the PLD process schematically and chamber along with laser used in the present work. An excimer laser (Coherent Compex Pro 102F) operating at a wavelength of 248 nm was used. The spherical deposition chamber (Excel Instruments, Mumbai) was fitted with a turbo molecular pump (Pfeiffer, Germany) and a base vacuum of 10^{-6} mTorr was achieved prior to deposition. The chamber had a substrate heater which could reach a temperature of 800 °C with resistive heating. In addition, the chamber was equipped with a target carousel which can accommodate six targets allowing for multilayer deposition without disturbing vacuum. The substrate holder was held parallel to the target material to achieve the maximum plume condensed on to substrate. The substrate holder to target distance was fixed to be 5 cm in the present study. Fused silica and Z-cut quartz (SiO_2) substrates were ultrasonicated in acetone solution and then dried to get impurity free substrate wafers. All deposition conditions such as laser fluence, partial pressure, substrate temperature and repetition rate for both Al:ZnO and LiNbO_3 are tabulated in Fig. 2. The samples are renamed as LN 01, LN 02 and LN 03 for simplicity.

2.3. Instrumentation details

Bruker X-ray diffractometer (Bruker D8 Discover with $\text{Cu K}\alpha = 1.5405$ Å source) was used to examine the crystallographic structure of the deposited LiNbO_3 and Al:ZnO thin films. In the present study, thickness and roughness of deposited thin films were carried out using a surface profilometer. Atomic Force Microscopy (AFM) (Model SPA400 of SII Inc, Japan-AFM) was used to extract the surface morphological details and the images were analyzed by Spiwin Lab analysis software. Microstructure of the films for grain structure and porosity were examined using Field Emission Scanning Electron Microscope (FE-SEM; Carl Zeiss, Ultra 55). The UV–vis absorption measurements were performed using a computer interfaced Jasco V-570 UV/VIS/NIR spectrophotometer. Photoluminescence (PL) and Raman scattering measurements were performed using a scanning near field optical microscopy (SNOM) equipped with a laser source of excitation wavelength 355 nm. We used a Raman spectrophotometer (Renishaw Invia Raman Microscope equipped with a Nd:YAG 532 nm laser) in the back scattering geometry in a CRM spectrometer furnished with a confocal microscope, 100X objective (1 μm diameter focal spot

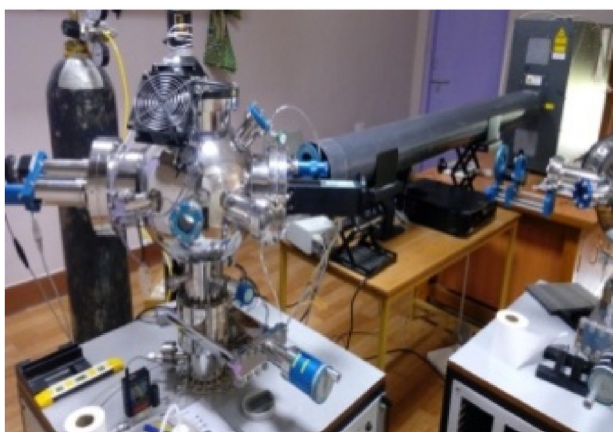
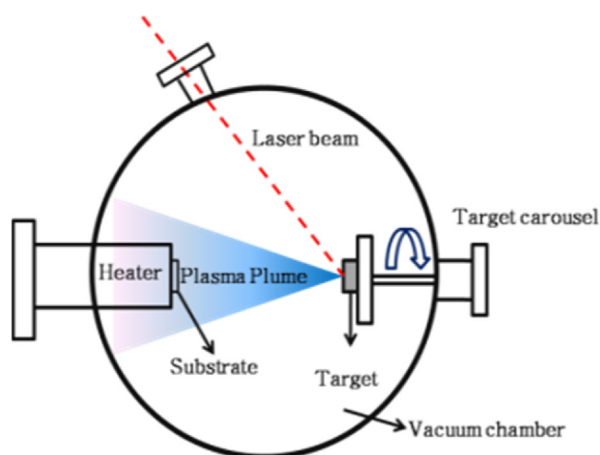


Fig. 1. Schematic (top view, left) and actual setup (right) of the pulsed laser deposition experiment.




	Substrate Temperature (°C)	Working Pressure (mbar)	Laser fluence (J/cm ²)	Repetition rate
 Polycrystalline LiNbO ₃ - LN 01	600	1.5×10^{-1}	1.52	5
 (110) oriented LiNbO ₃ - LN 02	600	1×10^{-1}	1.52	5
	100	1.5×10^{-1}	1.52	5
 (300) oriented LiNbO ₃ - LN 03	600	1×10^{-1}	1.52	5
	500	2×10^{-3}	1.52	5

Fig. 2. Schematic representation of substrate/ZnO/LiNbO₃ thin films used for the present study and their deposition conditions.

size) and a CCD detector (model alpha 300 of WiTec, Germany). The Z-scan experiments were performed with a mode locked Ti: sapphire laser at a repetition rate of 80 MHz at 800 nm. The input laser beam was spatially filtered to obtain a pure Gaussian profile in the far field. In a typical Z-scan experiment beam waist at focus was $\sim 25 \mu\text{m}$ corresponding to a Rayleigh range of 2.54 mm.

3. Results and discussion

3.1. Structural studies

XRD diffraction spectra of LiNbO₃ and Al:ZnO thin films are illustrated in Fig. 3. These studies show that all the peaks in LN01 correspond to LiNbO₃ and were found to be polycrystalline in nature. All the peaks were indexed based on JCPDS diffraction file #880289. The amorphous nature of the substrate and the annealing temperature (600 °C) allowed LiNbO₃ to grow as polycrystalline with multiple planes oriented in different

directions. LN02 had predominantly one diffraction peak centered at $2\theta \sim 34.6^\circ$ which corresponds to the (110) reflection from LiNbO₃ and underneath Al:ZnO grows in (002) direction. The Al:ZnO was deposited on fused silica under the minimal stress conditions at 100 °C oriented in (002) direction [27]. The peak positions of (002) Al:ZnO at 34.5° and (110) LN02 at 34.6° overlapped and was not distinguishable. LN03 deposited on Z-cut quartz with Al:ZnO as intermediate layer had only one peak at 62.9° . This peak also overlapped with the bottom layer Al:ZnO whose (103) plane originates at 62.7° (JCPDS diffraction file # 891397). Thus, Al:ZnO acted as a nucleating layer and controlled the growth of LiNbO₃ in the case of LN02 and LN03. In case of LN02, Al:ZnO was oriented in (002) and it was (103) in the case of LN03. In general, ZnO tends to grow in (002) preferred orientation because of its lowest surface energy in this plane [28]. The FWHM of (103) peak was larger than the (002) peak indicating the induced stress along (103) direction was larger than that of (002) direction. The main reason for stress is due to the lattice mismatch for LN03 whereas this can be ignored in

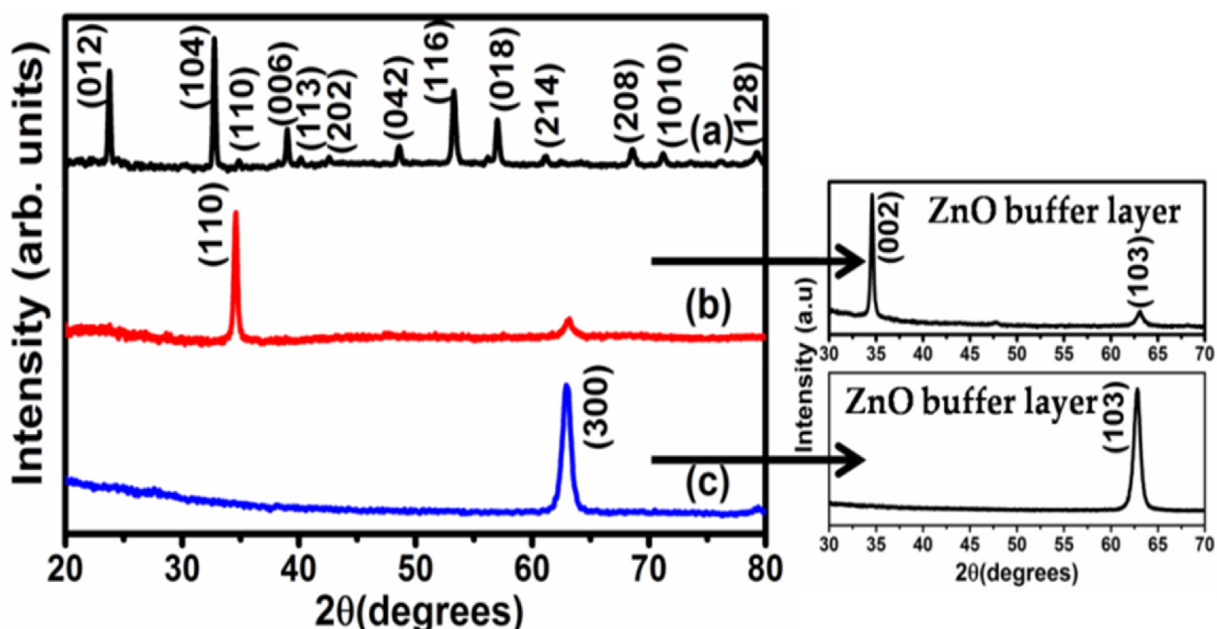


Fig. 3. XRD patterns and microstructure of (a) LN 01 (b) LN 02 (c) LN 03.

case of LN02. Another important reason for the stress is the substrate temperature of both the films deposited at 100 °C and 500 °C. Kumar et al. reported that at higher temperature, in Al:ZnO the (103) growth strongly dominated over the (002) [29]. This confirmed that Al:ZnO (103) oriented film deposited at 500 °C has lower surface free energy than (002) oriented film deposited at 100 °C. Based on the nature of substrate, substrate temperature, parameters such as laser fluence and partial pressure growth of LiNbO₃ can be optimized in preferred orientation.

3.2. Morphological details

Fig. 4 depicts the 2D and 3D AFM images along with microstructure obtained from the FE-SEM data of LN thin films. The surface morphology of LN 01 consisted of loosely packed grains with random orientation which can be confirmed from FE-SEM image also. LN 02 consisted of dense and well-structured grains. The (002) oriented Al:ZnO as an underlying layer controlled the morphology of LN whereas in the case of LN 01, the grains were distorted and not properly crystallized at 600 °C. In the case of LN 02, it can be inferred from the microstructure, that the grains were properly crystallized possessing uniform morphology. In the case of LN 03 the morphology was apparently different with elongated grains. In this case, LN 03 had Al:ZnO in (103) orientation where the stress induced to grow along (103) is larger when compared to (002) as discussed before. It can be confirmed from XRD data that the FWHM followed the trend of $FWHM_{LN01} < FWHM_{LN02} < FWHM_{LN03}$ which confirmed the increased stress in the case of

LN 03. The average roughness was found to be ~10 nm, ~7 nm and ~4 nm for LN 01, LN 02 and LN 03 samples, respectively. The roughness was observed to be descending for LN 01, LN 02 and LN 03. Therefore, the role of the substrate is predominant in the growth of bottom layer which ultimately decides the microstructure and growth of top layer.

3.3. UV-vis transmission spectra: band gap calculations

Fig. 5 illustrates the transmission spectra of LN films in the wavelength range of 200–1400 nm (visible-near IR) region. The oscillations in the spectra confirmed that the films were smooth and possessed uniform thickness. It can be deduced that the films exhibited good transparency in visible and near infrared region. In near IR, the average transmittance of all films was ~86% and decreased in visible region ranging from 78% to 86%. The LN02 and LN03 samples were more transparent compared to LN01. This might be because of the optical loss obtained from scattering of incident photon from grains and grain boundaries, porosity present in the polycrystalline film whereas the LN02 and LN03 had densely packed grains with lesser grain boundaries. The morphology of LN01, LN02 and LN03 confirmed the roughness of the films where the scattering of incident photons will be more in case of LN01 and less in case of LN02 and LN03 (Fig. 4).

The optical band gap (E_g) of the films was determined from Tauc's plot and are shown in Fig. 5. The single crystal LiNbO₃ exhibits a fundamental direct/indirect band gap of 4 eV [30]. The optical band gap of LiNbO₃ is detrimental to the valence electronic

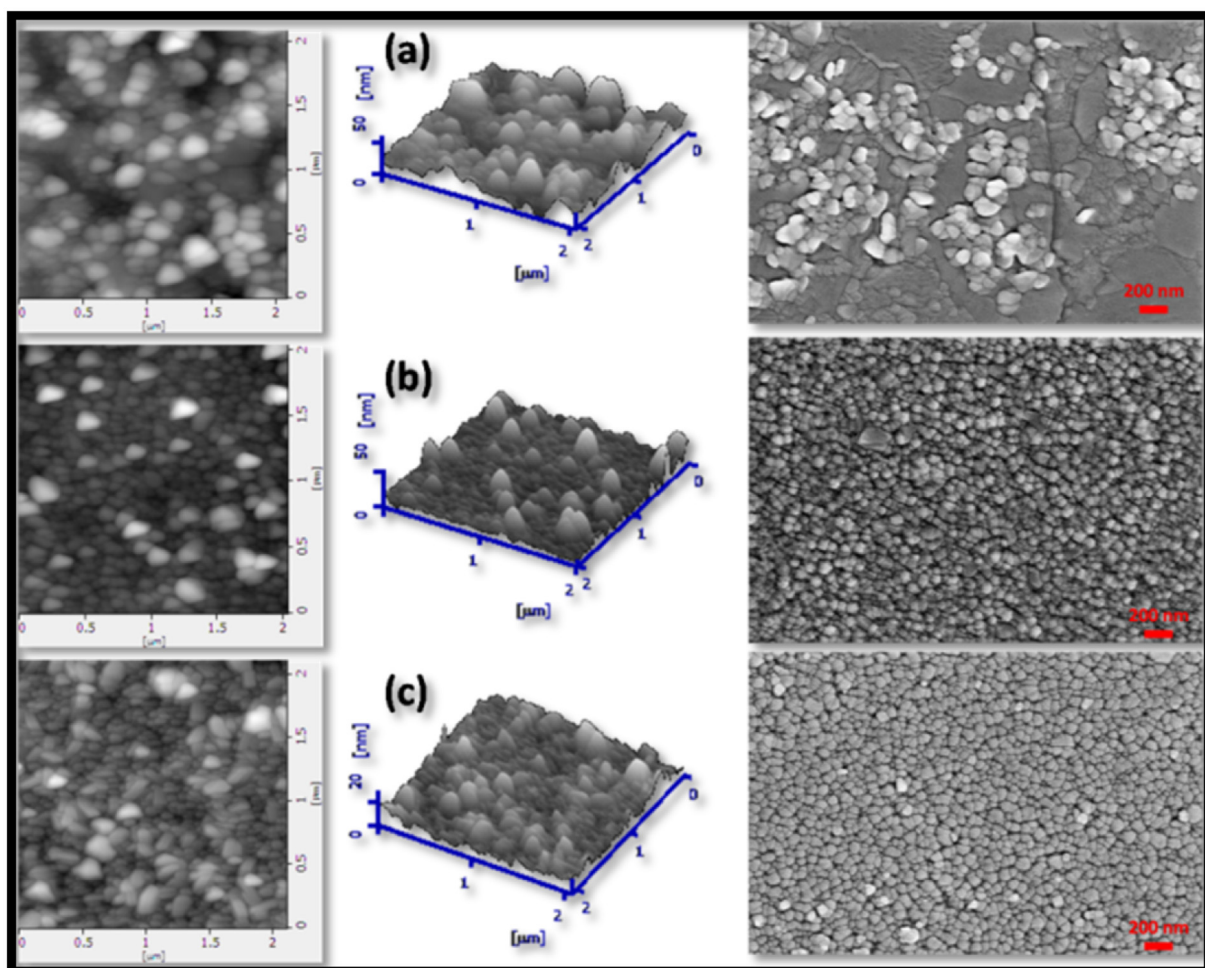


Fig. 4. AFM [2D (left) and 3D (middle)] and FE-SEM images [right] of microstructures for (a) LN 01 (b) LN 02 (c) LN 03.

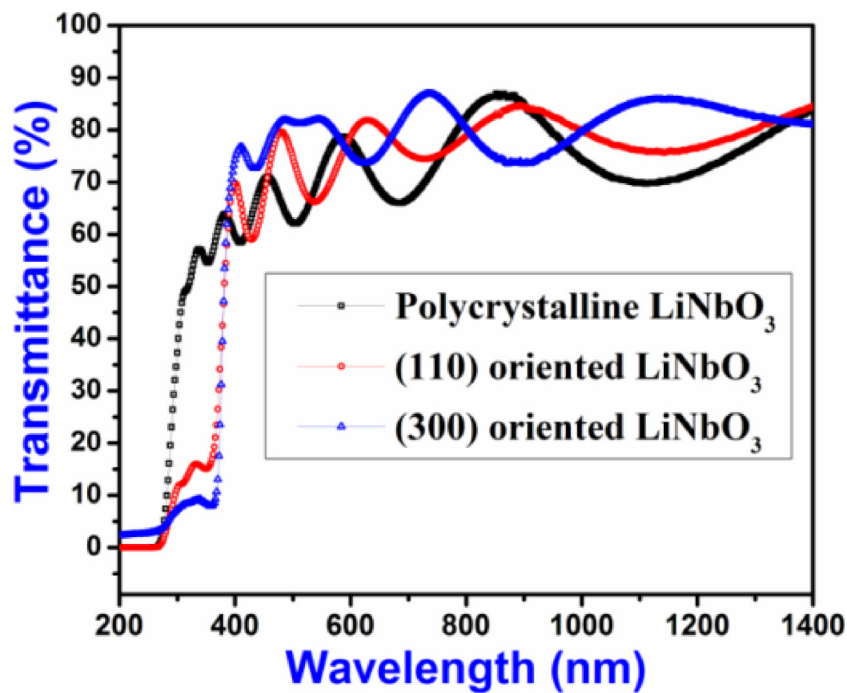


Fig. 5. Optical transmittance spectra of LN 01, LN 02 and LN 03.

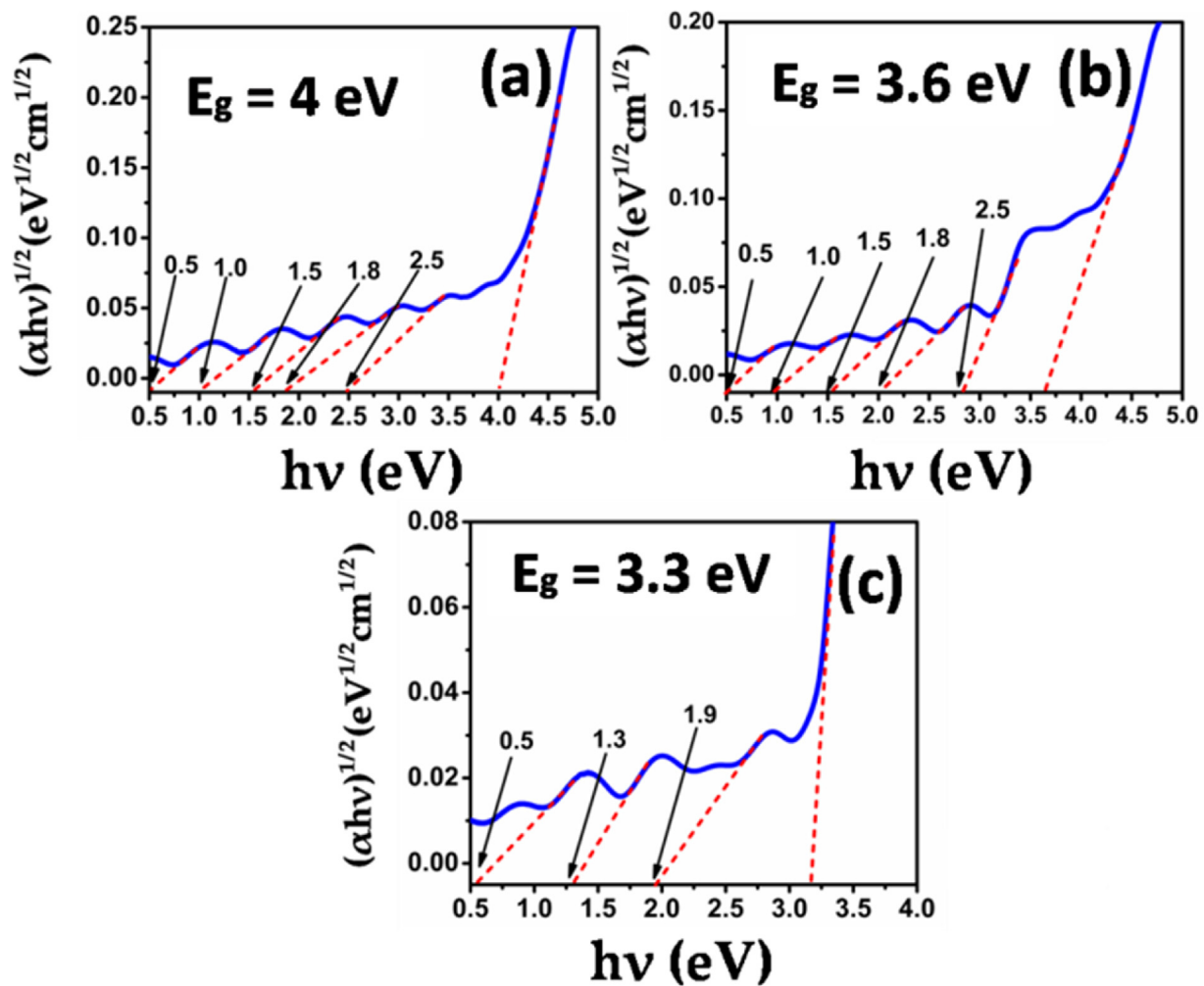


Fig. 6. Indirect band gap from Tauc's plot for (a) LN 01 (b) LN 02 (c) LN 03 (Asymmetric absorption humps at low energies from defect states are clearly marked with an arrow).

transitions from 2p orbitals of O^{2-} to the 4d orbitals of Nb^{5+} [31]. The distortion of the oxygen octahedron also depends on the concentration of intrinsic defects. This band gap either red shifts or blue shifts depending on the crystal orientation and growth technique and defect concentration [32]. Fig. 6 illustrates the indirect band gap plots of $LiNbO_3$ thin films and the data was analyzed to provide more insight in to the electronic transitions of $LiNbO_3$ in polycrystalline and oriented form. For LN01, LN02 and LN03 samples, a plot of ' α ' did not provide an exponential dependence on ' $h\nu$ '. Therefore, the low energy absorption edge observed from the transmittance data of Fig. 5 can be better interpreted as being due to the indirect absorption than due to the direct absorption. It is clear from Tauc's plot that the indirect band gap for all the films are ranging between 4 and 3.17 eV. The nature of band gap is indirect which can be confirmed from the absorption band edge of transmission spectra (Fig. 5).

Anil et al. recently reported the deposition of $LiNbO_3$ thin films using RF magnetron sputtering and found that the band gap varied with change in substrate annealing temperature [31]. Thierfelder et al. calculated the theoretical band gaps for ferro- and paraelectric states of $LiNbO_3$ from DFT calculations using the GW approximation [30]. The determination of optical band gap is obtained by Tauc's equation [33]

$$\alpha h\nu = A(h\nu - E_g)^n \quad (1)$$

where A is a constant, $h\nu$ is photon energy, E_g is the allowed energy gap, $n = 1/2$ for allowed direct transitions, $n = 2$ for allowed indirect transitions. From the indirect band gap plots, apart from the major absorption band edge, small unsymmetrical absorption band peaks centered at different energies were clearly observed which cannot be ignored. These absorption peaks were correlated with the defect centers or polaronic peaks which ultimately affect the linear and NLO properties [34]. The contribution of the polaronic states on NLO properties are discussed in detail in the ensuing section.

3.4. Photoluminescence spectra: emission studies

The PL spectra recorded for all the thin films with an excitation wavelength of 355 nm are depicted in Fig. 7. The emission wavelength was found to be distinct for LN 01, LN 02 and LN 03. LN 01 did not demonstrate any significant emission because of its higher band gap of 4 eV. The excitation wavelength was 355 nm which corresponds to ~ 3.5 eV and is not sufficient to excite the states of the structure. Broad emission peaks at 614 nm (red) and 558 nm (green) were observed in case of LN 02 and LN 03, respectively. In general, literature on emission from pure $LiNbO_3$ is limited [35]. The red and green emissions can be attributed due to the electronic transitions happened in the intermediate states near

1.0 eV (Nb_{Nb}^{4+}), 1.6 eV (Nb_{Li}^{4+}) and 2.5 eV (both Nb_{Nb}^{4+} and Nb_{Li}^{4+} and O^-). However, the emission mechanism cannot be explained solely based on the luminescence spectra. Efficient blue (473 nm) and green (505 and 525 nm) emissions were observed from polycrystalline $LiNbO_3$ ceramics doped with Sc_2O_3 and Lu_2O_3 [34]. Yakovlev et al. measured luminescence centers in $LiNbO_3$ crystals and explained the kinetics of color-center recombination due to different polaronic states which can be confirmed from the asymmetric absorption bands in Fig. 6 [36].

3.5. NLO studies with femtosecond laser pulses

The nonlinear absorption and refraction were examined for LN 01, LN 02 and LN 03 thin films using the open and closed aperture Z-scan techniques, respectively. Z-scan experiments were carried out with femtosecond (fs) laser pulses and the data is presented in Fig. 8. The thickness of all samples satisfied the Rayleigh range condition $L < n_0 Z_0$ where n_0 -linear refractive index at 800 nm, Z_0 - Rayleigh range, L is the thickness of sample. The substrate (fused silica and quartz) nonlinearity was recorded for reference and any minute contribution observed was subtracted for all the films. The OA Z-scan data was fitted to the two-photon absorption (2PA) and three-photon absorption (3PA) provided by using the Sheik-Bahae model [37] along with Eqs. (2) and (3), respectively. From OA fitted curve, nonlinear absorption coefficient (α_2) was calculated

$$T_{OA}(2PA) = 1/1 + \beta L_{eff} \left(I_{00}/1 + (Z/Z_0)^2 \right) \quad (2)$$

where effective path length $L_{eff}(2PA) = 1 - e^{-\alpha_2 L}/\alpha_2$

$$T_{OA}(3PA) = 1/[1 + 2\alpha_3 L_{eff} (I_{00}/(1 + (Z/Z_0)^2))]^{1/2} \quad (3)$$

$$L_{eff}(3PA) = 1 - e^{-2\alpha_3 L}/2\alpha_3 \quad (4)$$

I_{00} is the peak intensity, Z is the sample position, Z_0 is the Rayleigh range, β and α_3 are 2PA and 3PA coefficients.

Reverse saturable absorption (RSA) kind of behavior was observed in the case of LN 01 and LN 03 samples whereas saturable absorption (SA) was observed in the case of LN 02 sample. The optical band gap of all the films satisfies the condition that $2h\nu < E_g < 3h\nu$ ($h\nu = 1.55$ eV is the energy corresponding to photon at the incident laser wavelength of 800 nm), suggesting the occurrence of 2PA via intermediate virtual states [38] and these transitions are not directly into the conduction band but into the various defect states lying in the intermediate region of conduction and valence bands. The factors influencing the switching phenomenon from RSA to SA is the competition between the ground-state absorption and the nonlinear absorption mechanism, which further depends on the laser photon energy, the optical band

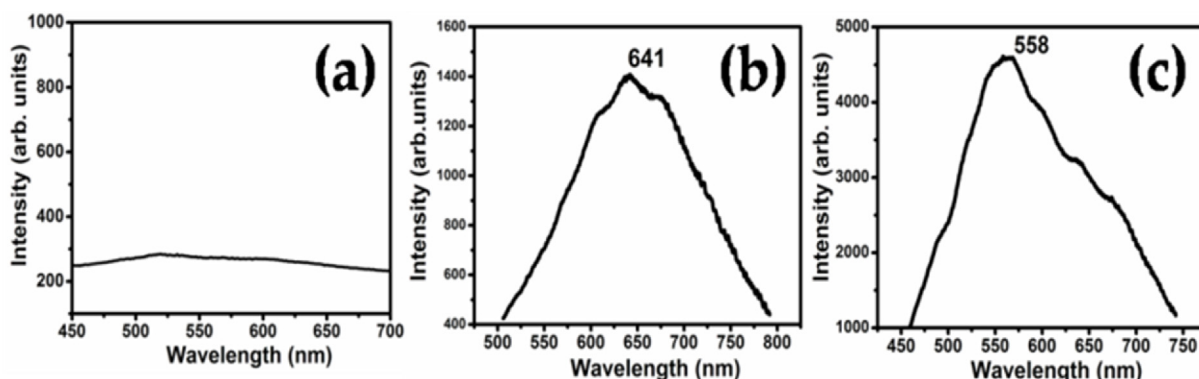


Fig. 7. Photoluminescence spectra for (a) LN 01 (b) LN 02 (c) LN 03.

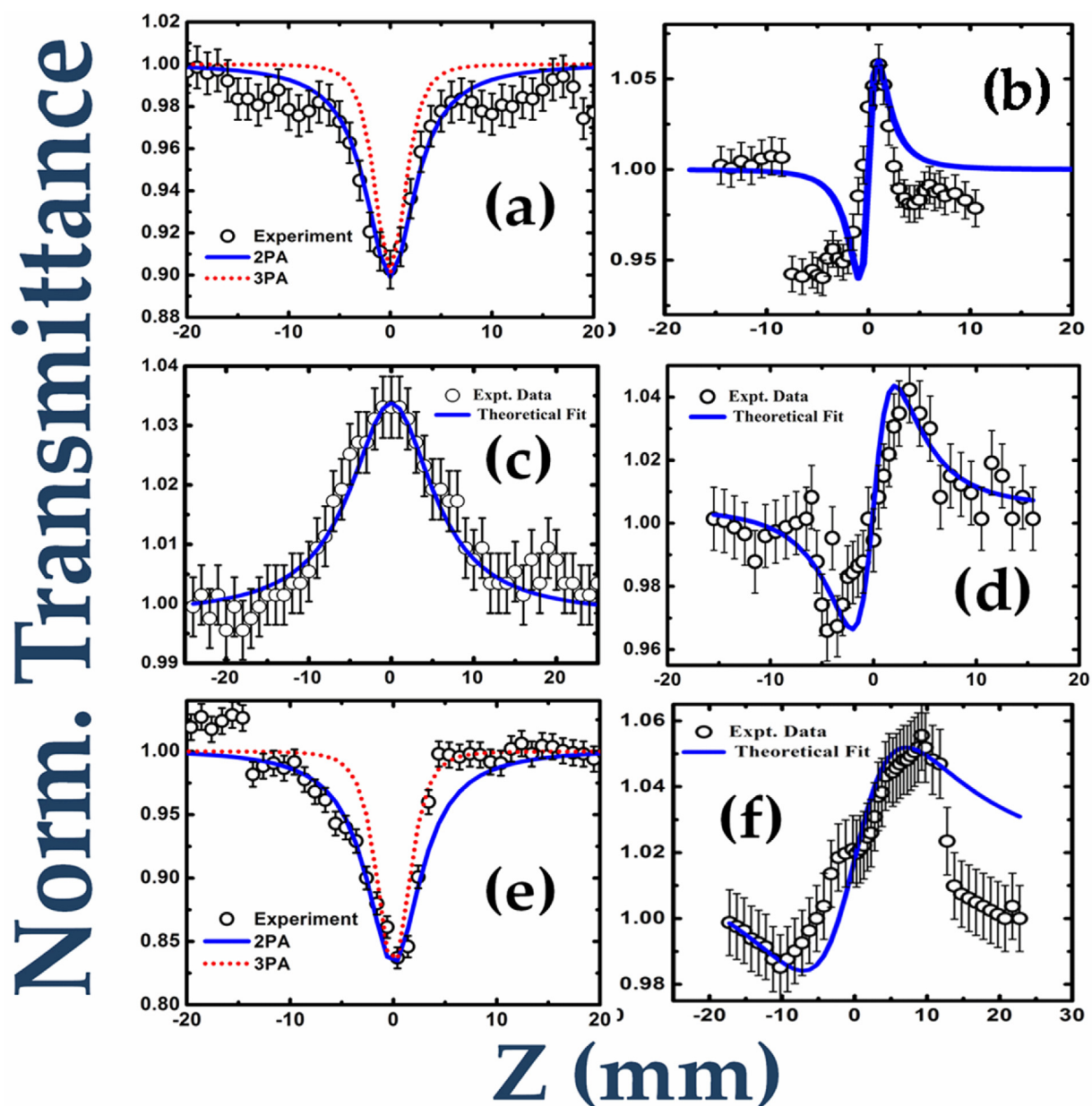


Fig. 8. OA [left] and CA [right] data of LN01 [(a), (b)] LN02 [(c), (d)] and LN03 [(e), (f)]. 2PA was best fit for LN 01 and LN 03 [blue solid lines are for 2PA and red dotted lines are for 3PA]. (For interpretation of the references to colour in this figure legend, the reader is referred to the web version of this article.)

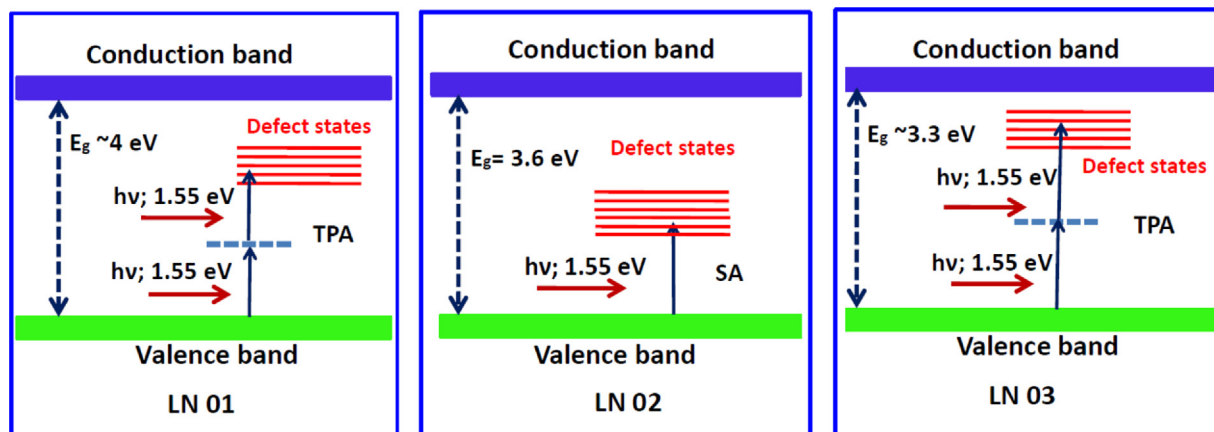


Fig. 9. Schematic diagram of nonlinear absorption process in LiNbO_3 thin films with varying band gaps (LN 01–4 eV, LN 02–3.6 eV, LN 03–3.3 eV).

gap of materials, the presence of intermediate defect states and intensity of the incident radiation [39]. In the present study, the Z-scan experiments were conducted at fixed intensity of incident radiation (I_0) and wavelength (λ). Therefore, the nonlinear optical absorption switching in LiNbO₃ thin films may be attributed to the changes occurred in optical band gap (E_g) due to structural indifferences. Even a small difference in E_g (<10 meV) is adequate for the transformation from RSA to SA [39]. In general, the intermediate defect states (energy levels) between valence and conduction bands act as barrier for the excited electrons to transit. When E_g is larger, it is difficult to excite electrons from defect states to conduction band through 2PA unless pumped with sufficiently high peak intensities. When E_g is small, more electrons can be allowed in to conduction band resulting in 2PA/RSA [40]. Furthermore, LN 03 possessed defect states with a band gap of 3.3 eV confirming the presence of 2PA. The unsymmetrical absorption humps from indirect Tauc's plot (Fig. 6) also confirmed the presence of defect states in LN 01, LN 02 and LN 03.

In case of LN 01 and LN 03, E_g was observed to be 4 eV and 3.6 eV whereas 2PA energy corresponds to 3.1 eV. When the films are away from the focus, the transmittance is high and as the sample translates towards focus, the transmittance decreases indicating RSA behavior. RSA is observed mainly because of the nonlinear mechanisms such as two-photon absorption (TPA), free carrier absorption (FCA), nonlinear scattering or a combination of these processes [41]. In LiNbO₃, the defect states are mainly attributed to the antisite defects like Nb replacement in Li site and oxygen vacancies [42]. In LiNbO₃, RSA is mainly dominated by TPA and the contribution from FCA can be highly ignored since the number of free carriers in LiNbO₃ is less where the observed indirect band gap is found to be between 4 and 3.3 eV. Furthermore, since the pulses used were ~ 150 fs in duration there is no scope for the presence of any excited state absorption. Despite the significant difference between E_g of LN 01 and 2PA energy, RSA behavior was observed. Fig. 9 depicts an approximate energy level diagram and the possible transitions for LN 01, LN 02, and LN 03 based on the observed nonlinear absorption data. This could be attributed to the density of defect states in the band gap. Furthermore, we have also estimated the saturation intensity (I_s) for the sample LN02 by appropriately fitting the open aperture data. The value of I_s was

estimated to be $\sim 10^9$ W/cm². Due to high repetition rate (80 MHz) of the laser pulses there is a possibility of some thermally induced nonlinearity to the overall observed nonlinearity. However, present data is insufficient to separate the contribution of this nonlinearity. Z-scan measurements with low repetition rate pulses need to be performed to measure the pure nonlinearities devoid of any kind of thermal contribution [43].

Fig. 10 shows the Raman spectra of all the three samples. The spectral peaks of LN 01 are well developed and sharp implying that the films were more crystalline when compared to LN 02 and LN 03. In the present study, E(TO) and A1(TO) modes with peak positions are labeled and are found to be in complete agreement with previous literature [44]. In general, a Raman peak at 520 cm⁻¹ is to be clearly visible because of the bottom Si based substrate and is not dominant in LN 01, LN 02 and LN 03. The Raman peaks from buffer layer Al:ZnO also reflects in case of LN 02 and LN 03. The introduction of Al in ZnO changes the concentration of defects and can be better analyzed with additional active Raman modes. It can be understood that the peaks at 437 cm⁻¹ and 582 cm⁻¹ corresponds to Al:ZnO which overlaps with LiNbO₃ standard Raman peaks in case of LN 02 and LN 03. The intensities of these two peaks are quite less when compared to LN 01. This confirms that the influence of Al:ZnO cannot contribute much to the changes observed in properties of LiNbO₃ thin films (LN 02 and LN 03). Therefore, it is difficult to distinguish Raman peaks of LiNbO₃ from Al:ZnO in case of LN 02 and LN 03. The presence of dense defect states can be confirmed from the intensities of A1(LO4) and E(TO1) Raman peaks (data presented in Fig. 10). The defect states in LiNbO₃ were prominent in the case of LN 01 and LN 03 whereas the same were not pronounced in the case of LN 02 [43]. SA was observed for LN 02 where E_g is lower compared to LN 01. Generally, when E_g is low, the possibility of electrons to jump from valence band to low lying defect states exists. This results in absorption saturation of defect states and subsequently in SA behavior. This might be because of the presence of adequate density of defect states. Such behavior has not been reported previously in ferroelectric thin films [45].

Another probable reason for the observation of RSA and SA can be explained based on movement of polaronic states in LiNbO₃. The indirect band gap of LN 03 is ~ 3.3 eV where the contribution to

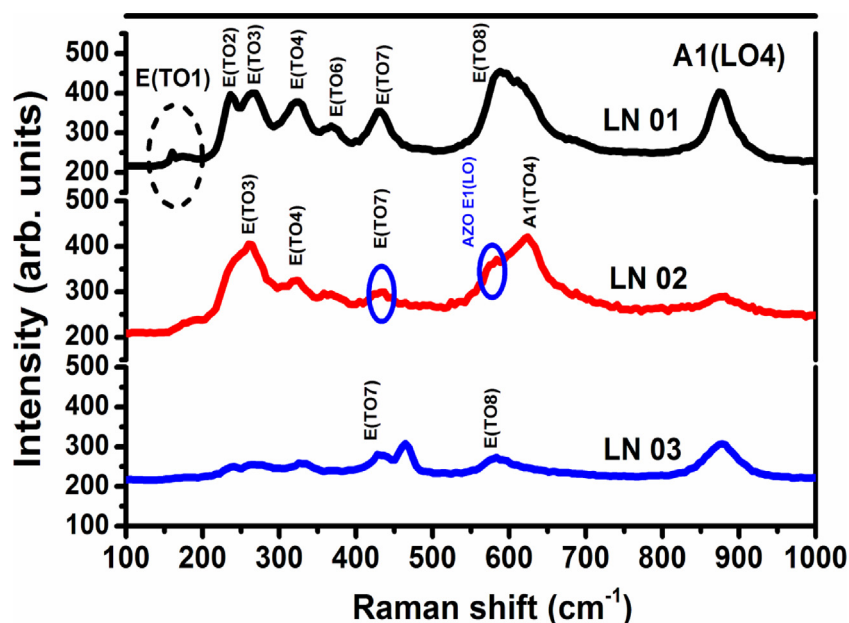


Fig. 10. Raman spectra recorded for LN01, LN02 and LN03.

nonlinearity arises from the presence of small polarons and bipolarons. In general, the manifestations of small polarons affect strongly the linear and nonlinear optical properties in LiNbO₃ crystal [34]. Till now, three different small electron polarons and one type of small hole polaron have explicitly been identified in LiNbO₃. These polarons show strong absorption bands near 1.0 eV (Nb_{Nb}^{4+}), 1.6 eV (Nb_{Li}^{4+}) and 2.5 eV (both Nb_{Nb}^{4+} and O^-) [34]. These absorption bands are asymmetric in nature with typical half widths of 1 eV. The presence of these bipolarons can be confirmed from Tauc's plot (Fig. 6) where asymmetric absorption peaks at lower energies were present. Small polaron absorption is proportional to the product of number density and their absorption cross section. The values of nonlinear absorption coefficient (β) of LN 01, LN 02 and LN 03 are summarized in Table 1. It is evident that for LN 01 and LN 03 positive β was observed and in case of LN 02 saturable absorption was observed. The β value was slightly higher in the case of LN 03 when compared to LN 01. To cross check the obtained results, 3PA equation was fitted for OA data of LN 01 and LN 03 as shown in Fig. 7. But, the 3PA curves did not fit well with the experimental data confirming the presence of 2PA only.

Fig. 8 illustrates the CA Z-scan data of LN 01, LN 02 and LN 03 films. The intense valley followed by a peak was observed while moving the sample through the focal point. This indicates the positive sign associated with the nonlinear refraction accompanied by nonlinear absorption.

$$T_{CA} = 1 - \frac{4\Delta\phi_o(Z/Z_o)}{[1 + (Z/Z_o)^2][9 + (Z/Z_o)^2]} \quad (5)$$

$\Delta\phi_o$ is the phase change of the laser beam due to nonlinear refraction and is estimated by fitting the experimental data, Z is the position of sample, Z_o is the Rayleigh range.

$$n_2(\text{cm}^2/\text{W}) = \frac{|\Delta\phi_o|\lambda}{2\pi I_{00} L_{\text{eff}}} \quad (6)$$

For excitation with fs laser pulses the contribution of electrostriction, population redistribution effects and molecular reorientation towards nonlinear refractive index can be ignored since these effects have a larger response time greater than the order of few hundreds of fs. Therefore, the large refractive nonlinearity of LiNbO₃ thin films recorded in the fs range should result from third order polarization $P^{(3)}$ which includes electronic polarization P_e and ferroelectric polarization P_f . The electronic polarization results from the deformation of electron cloud. The ferroelectric polarization is strongly coupled to strain and temperature. Therefore, strain tuning of ferroelectric polarization in perovskites (LiNbO₃) further induces polarization reversal in LiNbO₃ thin films. Another important reason is the enhancement of strain in the film which further increases the ferroelectric polarization. The ultrashort laser pulses induce polarization reversal in lattice generating ultrafast strain thereby enhancing ferroelectric polarization [46]. LN 01 and LN 02 possessed relatively less strain when compared to LN 03 which has been confirmed from XRD (Fig. 2). The ultrashort laser pulses allow the dipoles to reorient themselves more in the case of LN 01 since it is polycrystalline and less in the case of LN 02

and LN 03 which were oriented in the (110) and (300) directions, respectively. Therefore, the contribution of polarization reversal towards the nonlinear refractive index follows the trend of LN 02 > LN 01 > LN 03.

For calculating the real and imaginary parts of third-order optical nonlinearity, $[\text{Re}|\chi^{(3)}|$ and $[\text{Im}|\chi^{(3)}|]$ values Eq. (7) and (b) were used and the values of $|\chi^{(3)}|$ were extracted. NLO coefficients such as real and imaginary parts of susceptibility, nonlinear absorption coefficient and refractive index are summarized in the Table 1. Third-order NLO coefficients of LiNbO₃ for single crystal and thin films reported in literature till date [47–50] are provided in the Table 2. The NLO coefficients depend strongly on several factors such as input laser pulse duration, fluence, wavelength, repetition rate etc. and it not appropriate to directly compare the obtained coefficients in this work with those obtained with different input conditions or growth parameters. The conversion of bulk to nano-dimensions will enhance the nonlinear coefficients [51]. The data obtained from our NLO measurements are reproducible with an estimated error of $\pm 25\%$ due to the very thin nature of the sample, input laser fluctuations, estimation of the peak intensities and fitting errors. We did not observe any nonlinearity from the substrates and Al:ZnO as well (for the similar input powers used).

$$\text{Re}|\chi^{(3)}|(\text{esu}) = \frac{10^{-4}\epsilon_o n_o^2 c^2}{\pi} n_2 \left(\frac{\text{m}^2}{\text{W}} \right) \quad (7)$$

$$\text{Im}|\chi^{(3)}|(\text{esu}) = \frac{10^{-2}\epsilon_o n_o^2 c^2 \lambda}{4\pi^2} \beta \left(\frac{\text{m}}{\text{W}} \right) \quad (8)$$

n_o - Refractive index of solvent, n_2 - Refractive index of material, ϵ_o - Permittivity of free space, c - velocity of light

$$|\chi^{(3)}|(\text{esu}) = \sqrt{[\text{Re}|\chi^{(3)}|]^2 + [\text{Im}|\chi^{(3)}|]^2} \quad (9)$$

4. Conclusions

In conclusion LiNbO₃ thin films were deposited using pulsed laser deposition technique. Third order NLO properties of the films were investigated using the Z-scan technique at a wavelength of 800 nm. Positive nonlinearity was observed for polycrystalline LiNbO₃ and (300) LiNbO₃. Two-photon absorption was observed in two samples while the third one depicted saturable absorption. The polycrystalline LiNbO₃ and (300) LiNbO₃ exhibited 2PA and that changed to SA in the case of (110) LiNbO₃. The magnitude of the nonlinear susceptibility for all the films was $\sim 10^{-11}$ e.s.u. which is orders of magnitude higher than that of the single crystal Z-cut LiNbO₃. The high optical transparency and third order optical nonlinearity show that LiNbO₃ thin films are promising candidates for nonlinear photonic devices. SA phenomenon can be used for ultrafast optical modulation in the laser oscillators to generate ultrashort laser pulses and 2PA is a typical characteristic required for optical limiting devices (sensors) which is seldom reported in LiNbO₃ thin films. The obtained results on third order nonlinearity

Table 1
Nonlinear optical parameters calculated for LiNbO₃ thin films.

Sample	β (cm/W) $\times 10^{-8}$	n_2 (cm ² /W)	$\text{Re} \chi^{(3)} $ (esu)	$\text{Im} \chi^{(3)} $ (esu)	$ \chi^{(3)} $ (esu)
LN 01	125	1.7×10^{-9}	2.3×10^{-11}	1.1×10^{-11}	2.5×10^{-11}
LN 02	-217	2.9×10^{-9}	3.9×10^{-11}	1.9×10^{-11}	4.3×10^{-11}
LN 03	165	1.1×10^{-10}	1.5×10^{-12}	1.4×10^{-11}	2.0×10^{-11}

Table 2Comparison of third order nonlinear optical parameters of LiNbO₃ reported so far.

LiNbO ₃ form	Wavelength/Pulse duration/Rep. rate	Nonlinear absorption coefficient (β)	Nonlinear refractive index (n ₂)	Nonlinear susceptibility (χ ⁽³⁾)	References
LiNbO ₃ thin film from RF magnetron sputtering	532 nm/–/10 Hz	-7.2×10^{-9} cm/kW	0.39 cm ² /W	9.1×10^{-7} e.s.u.	[16]
Z-cut LiNbO ₃ crystal	514 nm/–/10 Hz	–	0.67×10^{-7} cm ² /W	–	[47]
Chemically reduced pure LiNbO ₃ crystals	644 & 514 nm/–/–	0.45×10^{-3} cm/kW	–	–	[24]
Pure LiNbO ₃ single crystal	1064 & 532 nm/55 ps/2 Hz	2.1×10^{-10} cm/W	–	–	[48]
Periodically poled LiNbO ₃	770 nm/25 ps/10 Hz	6.0×10^{-12} cm/W	–	–	[49]
LiNbO ₃ single crystal	532 nm/25 ps/10 Hz	2.5×10^{-10} cm/W	5.3×10^{-15} cm ² /W	7.45×10^{-13} e.s.u.	[50]

and their behavior are also of interest because of its cost-effective applications in optical devices.

Acknowledgements

Mr. Anil Tumuluri would like to acknowledge Ms. Mounika Rapolu and Dr. Syed Hamad for their assistance in recording the NLO data and help in fitting the Z-scan data. Authors would also like to thank School of Physics, University of Hyderabad for extending the experimental facilities. S.V. Rao acknowledges the financial support of DRDO, India.

References

- [1] H. Nili-Ahmadabadi, A.R. Khorsandi, Chin. Phys. B 20 (2011) 5.
- [2] Md. Rashedul, H. Sarker, H. Karim, R. Martinez, D. Delfin, R. Enriquez, M. Arif, I. Shuvo, N. Love, Y. Lin, Measurement 75 (2015) 104.
- [3] H. Lu, B. Sadani, N. Courjal, G. Ulliac, N. Smith, V. Stenger, M. Collet, F.I. Baida, M. P. Bernal, Opt. Express 20 (2012) 2974.
- [4] M. Bazzan, C. Sada, Appl. Phys. Rev. 2 (2015) 040603.
- [5] S. Sanna, W.G. Schmidt, Phys. Rev. B 81 (2010) 214116.
- [6] R.R. Thomson, S. Campbell, I.J. Blewett, A.K. Kar, D.T. Reid, Appl. Phys. Lett. 88 (2006) 111109.
- [7] P. Mackwitz, M. Rüsing, G. Bert, A. Widhalm, K. Müller, A. Zrenner, Appl. Phys. Lett. 108 (2016) 152902.
- [8] L. Cai, R. Kong, Y. Wang, H. Hu, Opt. Express 23 (2015) 29211.
- [9] M.F. Volk, S. Suntsov, C.E. Rüter, D. Kip, Opt. Express 2 (2016) 1386.
- [10] G. Balestrino, S. Martellucci, P.G. Medaglia, A. Paoletti, G. Petrocelli, A. Tebano, A. Tucciarone, F. Gelli, E. Giorgetti, S. Sottini, L. Tapfer, Appl. Phys. Lett. 78 (2001) 1204.
- [11] A. Bartasyte, S. Margueron, T. Baron, S. Oliveri, P. Barlet, Adv. Mater. Interfaces 4 (2017) 1600998.
- [12] A.V. Prasada Rao, D.S. Paik, S. Komarneni, J. Electrocer. 2 (1998) 157.
- [13] K. Nashimoto, M.J. Cima, Mater. Lett. 10 (1991) 348.
- [14] A. Iyevlev, M. Kostyuchenko, V. Sumets, J. Vakhtel, J. Mater. Sci.: Mater. Electron. 22 (2011) 1258.
- [15] P. You, C. Lu, W. Ye, L. Hao, J. Zhu, Y. Zhou, Appl. Phys. Lett. 102 (2013) 051914.
- [16] S. Shandilya, M. Tomar, K. Sreenivas, V.J. Gupta, Appl. Phys. Lett. 105 (2009) 4105.
- [17] Q.-Q. Wang, J. Shi, B.-F. Yang, H.-L. Liu, G.-G. Xiong, Q.-H. Gong, Q.-K. Xue, Chin. Phys. Lett. 19 (2002) 677.
- [18] K. Venkata Saravanan, K.C. James Raju, M. Ghanashyam Krishna, Surya P. Tewari, S. Venugopal Rao, Appl. Phys. Lett. 96 (2010) 232905.
- [19] M. Sukumar, R. Ramesh Babu, K. Ramamurthi, Appl. Phys. B 121 (2015) 369.
- [20] N. Setter, D. Damjanovic, L. Eng, G. Fox, S. Gevorgian, S. Hong, A. Kingo, H. Kohlstedt, N.Y. Park, G.B. Stephenson, I. Stolitchnov, A.K. Tagansteve, D.V. Taylor, T. Yamada, S. Streiffer, J. Appl. Phys. 100 (2006) 051606.
- [21] N.B. Gharb, S. Trolier-McKinstry, D. Damjanovic, J. Appl. Phys. 100 (2006) 044107.
- [22] E. Østreng, H.H. Sønsteby, T. Sajaavaara, O. Nilsen, H. Fjellvåg, J. Mater. Chem. C 1 (2013) 4283.
- [23] A. Tumuluri, M. Rapolu, S. Venugopal Rao, K.C. James Raju, AIP Conf. Proc. 2016 (1728) 020365.
- [24] S. Shandilya, M. Tomar, V.J. Gupta, Appl. Phys. Lett. 111 (2012) 102803.
- [25] S.M. Kostritskii, M. Aillerie, J. Appl. Phys. 111 (2012) 103504.
- [26] F.Z. Henari, K. Cazzini, F. El Akkari, W.J. Blau, J. Appl. Phys. 78 (1995) 1373.
- [27] J.-P. Xu, S.-B. Shi, L. Li, X.-S. Zhang, Y.-X. Wang, X.-M. Chen, Chin. Phys. Lett. 27 (2010) 047803.
- [28] Y. Wang, X. Li, G. Jiang, W. Liu, C. Zhu, J. Mater. Sci.: Mater. Electron. 24 (2013) 3764.
- [29] A. Kumar, P. Kumar, K. Kumar, T. Singh, R. Singh, K. Asokan, D. Kanjilal, J. Alloys Comp. 649 (2015) 1205.
- [30] C. Thierfelder, S. Sanna, A. Schindlmayr, W.G. Schmidt, Phys. Status Solidi C 7 (2010) 362.
- [31] Anil Tumuluri, K.C. James Raju, Adv. Mat. Lett. 5 (2014) 287.
- [32] R. Sangeetha, S. Muthukumar, J. Mater. Sci.: Mater. Electron. 26 (2015) 9667.
- [33] B.D. Vezbick, S. Patel, B.E. Davis, D.P. Birnie, Phys. Status Solidi B 2015 (1700) 252.
- [34] M. Imlau, H. Badorreck, C. Merschjann, Appl. Phys. Rev. 2 (2015) 040606.
- [35] Anil Tumuluri, K.C. James Raju, Ceram. Int. 40 (2014) 3371.
- [36] V.Yu. Yakovlev, E.V. Kabanova, T. Weber, P. Paufler, Phys. Solid State 43 (2001) 1580.
- [37] M. Sheik-Bahae, A.A. Said, T.-H. Wei, D.J. Hagan, E.W. Van Stryland, IEEE J. Quantum Electron. 26 (1990) 76.
- [38] S. Li, X.L. Zhong, G.H. Cheng, X. Liu, J.B. Wang, J. Huan, J.H. Song, C.B. Tan, B. Li, Y. C. Zhou, Appl. Phys. Lett. 105 (2014) 192901.
- [39] B.S. Kalanoor, L. Gouda, R. Gottesman, S. Tirosh, E. Haltzi, A. Zaban, Y.R. Tischler, ACS Photonics 3 (2016) 361.
- [40] S. Pramodini, Y.N. Sudhakar, M. Selva Kumar, P. Poornesh, Laser Phys. 24 (2014) 4.
- [41] P.T. Anusha, A.R. Thomas, R. Philip, S. Venugopal Rao, Chem. Phys. Lett. 641 (2015) 23.
- [42] S. Shandilya, M. Tomar, K. Sreenivas, V.J. Gupta, J. Appl. Phys. 105 (2009) 094105.
- [43] E.D. D'Silva, G. Krishna Podagatlapalli, S. Venugopal Rao, S.M. Dharma Prakash, Mater. Res. Bull. 47 (2012) 3552–3557.
- [44] M.D. Fontana, P. Bourson, Appl. Phys. Rev. 2 (2015) 040602.
- [45] M.K. Gupta, N. Sinha, B. Kumar, J. Appl. Phys. 112 (2012) 014303.
- [46] K. McCash, A. Srikanth, I. Ponomareva, Phys. Rev. B 86 (2012) 214108.
- [47] S.M.G. Rabbani, S.M. Sharifi, Y. Haque, S.K. Das, N. Chawdhury, SUST J. Sci. Technol. 16 (2012) 2.
- [48] R.A. Ganeev, I.A. Kulagin, A.I. Rysanyanskii, R.I. Tugushev, T. Usmanov, Opt. Spectrosc. 94 (2003) 561.
- [49] M. Cherchi, S. Stivala, A. Pasquazi, A.C. Busacca, S.R. Saneverino, A.C. Cino, L. Colace, G. Assanto, Appl. Phys. B 93 (2008) 559.
- [50] H. Li, F. Zhau, X.W. Ji, App. Phys. B 64 (1997) 659.
- [51] C. Babeela, S. Venugopal Rao, R. Madhura Somayaji, T. Sabari Girisun, Mater. Res. Bull. 87 (2017) 102–108.